

Title	Aligning VLBI images of active galactic nuclei at different frequencies
Authors	Croke, S. M.; Gabuzda, Denise
Publication date	2008
Original Citation	Croke, S. M. and Gabuzda, D. C. (2008) 'Aligning VLBI images of active galactic nuclei at different frequencies', Monthly Notices of the Royal Astronomical Society, 386(2), pp. 619-626. doi: 10.1111/j.1365-2966.2008.13087.x
Type of publication	Article (peer-reviewed)
Link to publisher's version	<a href="https://academic.oup.com/mnras/article-lookup/doi/10.1111/j.1365-2966.2008.13087.x">https://academic.oup.com/mnras/article-lookup/doi/10.1111/j.1365-2966.2008.13087.x</a> - 10.1111/j.1365-2966.2008.13087.x
Rights	© 2008, the Authors. Journal compilation © 2008, RAS
Download date	2023-05-05 13:37:52
Item downloaded from	<a href="http://hdl.handle.net/10468/4975">http://hdl.handle.net/10468/4975</a>

# Aligning VLBI images of active galactic nuclei at different frequencies

S. M. Croke<sup>1,2</sup> and D. C. Gabuzda<sup>3★</sup>

<sup>1</sup>*Department of Physics, University of Strathclyde, Glasgow G4 0NG*

<sup>2</sup>*Department of Mathematics, University of Glasgow, Glasgow G12 8QW*

<sup>3</sup>*Department of Physics, University College Cork, Cork, Ireland*

Accepted 2008 February 6. Received 2008 January 10; in original form 2007 September 8

## ABSTRACT

Many important techniques for investigating the properties of extragalactic radio sources, such as spectral-index and rotation-measure mapping, involve the comparison of images at two or more frequencies. In the case of radio interferometric data, this can be done by comparing the CLEAN maps obtained at the different frequencies. However, intrinsic differences in images due to the frequency dependence of the radio emission can be distorted by additional differences that arise due to source variability (if the data to be compared are obtained at different times), image misalignment, and the frequency dependence of the sensitivity to weak emission and the angular resolution provided by the observations (the resolution of an interferometer depends on the lengths of its baselines in units of the observing wavelength). These effects must be corrected for as best as possible before multifrequency data comparison techniques can be applied. We consider the origins for the aforementioned factors, outline the standard techniques used to overcome these difficulties, and describe in detail a technique developed by us, based on the cross-correlation technique widely used in other fields, to correct for misalignments between maps at different frequencies.

**Key words:** techniques: image processing – galaxies: active.

## 1 INTRODUCTION

The radio emission of core-dominated, radio-loud active galactic nuclei (AGN) is synchrotron radiation generated in the relativistic jets that emerge from the nucleus of the galaxy, presumably along the rotational axis of a central supermassive black hole. One important source of information about the physical conditions in the radio-emitting regions is the distribution of the spectral index  $\alpha$  over the source ( $S_\nu \propto \nu^\alpha$ , where  $S_\nu$  is the source flux at frequency  $\nu$ ). The core region is typically observed to be at least partially optically thick, with a nearly flat or inverted spectrum, while the jets are optically thin, with negative spectral indices. The spectrum may also flatten in regions of the jet in which there is re-acceleration of electrons or low-frequency absorption (e.g. Gabuzda, Pushkarev & Garnich 2001a; Gabuzda, Gómez & Agudo 2001b). Synchrotron radiation can be highly linearly polarized, to  $\simeq 75$  per cent in the case of a uniform magnetic field (Pacholczyk 1970), and linear polarization observations can yield unique information about the orientation and degree of order of the magnetic field in the synchrotron source, as well as the distribution of thermal electrons and the magnetic field geometry in the immediate vicinity of the AGN (e.g. via Faraday rotation of the plane of polarization).

The compact radio emission of such AGN can be probed with high resolution using very long baseline interferometry (VLBI). The ra-

dio telescopes in the interferometric array can be separated by hundreds or thousands of kilometres, making it infeasible to physically link (synchronize) them electronically, and high-accuracy timing signals must be recorded together with the data, so that the signals obtained at different antennas can be accurately synchronized during correlation. In practice, the amplitudes and, especially, phases of the measured complex visibility data unavoidably contain unknown errors, which can conveniently be expressed via antenna-based complex gain factors:

$$V_{ij}^{\text{obs}} = G_i G_j^* V_{ij}^{\text{true}},$$

where  $V_{ij}^{\text{obs}}$  and  $V_{ij}^{\text{true}}$  are the observed and true visibility functions on the baseline between antennas  $i$  and  $j$ , and  $G_i, G_j$  are the complex gain factors for antennas  $i$  and  $j$ . The complex gains  $G$  must be determined and removed from the data in order to achieve the highest quality images possible for the radio-telescope array used. This is normally done iteratively, via alternate application of self-calibration (Fort & Yee 1976; Cotton 1979; Readhead & Wilkinson 1978; Readhead et al. 1980; Cornwell & Wilkinson 1981) and a deconvolution method, such as CLEAN (Högbom 1974).

## 2 MATCHING AND ALIGNING IMAGES AT DIFFERENT FREQUENCIES

Since AGN are variable, it goes without saying that multifrequency data to be compared must correspond to epochs separated by time

★E-mail: gabuzda@phys.ucc.ie

intervals appreciably less than the time-scales for variability of the source. When preparing data for techniques involving comparison of multifrequency data, various instrumental differences between the data sets must also be taken into account. VLBI data sets at different frequencies will have different angular resolutions and sensitivities to structures on various scales due to the different baseline coverages of the observations. One approach to reducing these differences when comparing multifrequency images is to match the baseline coverages at different frequencies by giving relatively low weights to the longest baselines at higher frequencies and to the shortest baselines at lower frequencies, e.g. via tapering of the visibility data. Alternatively, the images can be obtained without such weighting, but then all be convolved with the same CLEAN beam before comparison. The size of the CLEAN beam to be used in this case is ordinarily roughly equal to the central lobe of the dirty beam for the lowest frequency. The accuracy to which the positions of the CLEAN components are known is limited by the resolution of the observing system, and convolving with a beam that was much smaller than the central lobe of the dirty beam would result in a ‘super-resolved’ image that may not be reliable.

Iterative imaging via self-calibration and a deconvolution algorithm such as CLEAN is generally quite effective, but the absolute information about the coordinates of the source on the sky is lost during phase self-calibration, which essentially places the centre of gravity of the radio brightness distribution at the phase centre, which has coordinates (0,0). Because most radio-loud AGN are highly core-dominated, directly comparing multifrequency self-calibrated VLBI images of AGN essentially amounts to aligning these images on the observed VLBI core, which usually coincides very closely with the peak of the radio brightness distribution.

However, the standard theory of extragalactic radio sources (e.g. Blandford & Königl 1979) predicts a frequency-dependent shift in the location of the VLBI core due to opacity effects in the core region. Re-absorption of synchrotron radiation takes place in the ultracompact region near the central engine of an AGN, a mechanism which is more efficient at low frequencies. Consequently, the peak brightness appears further along the jet axis in lower frequency observations. Thus the alignment of multifrequency images on their VLBI core results in a misalignment between images of different observing frequencies. This prediction is supported by observation: the frequency-dependent shift in core position has been measured for several quasars and microquasars (see Lobanov 1998, and references therein), and the effect is discussed in terms of its impact on high-precision astrometry by Fey (2000), Charlot (2002), Ros (2005) and Boboltz (2006). Lobanov (1998) explains in detail how the frequency-dependence of the shift depends on physical conditions near the central engine.

It is thus necessary to correctly align images prior to applying multifrequency data analysis techniques. This can be achieved in one of two ways. The first is by phase-referenced observations, first employed by Marcaide & Shapiro (1984), in which a nearby source (or sources) is observed along with the target source. The reference source would ideally be a point source, to eliminate structure effects including those discussed above, but this is rarely possible since most sources show extended structure on the milliarcsecond scales available with VLBI. The position of the target source relative to the reference source can then be determined. The second method involves aligning images according to the positions of optically thin jet components (i.e. components optically thin to synchrotron radiation, so that their positions are not affected by absorption effects such as those occurring in the core) that are present in both images to be compared. This can be non-trivial, particularly if the source has a

complicated structure, but has been employed effectively by several authors, such as Paragi, Fejes & Frey (2000), who used this method to determine the radio core shift in 1823+568. This difficulty in aligning complex images without distinct optically thin components detected at all frequencies to be compared was the main motivation for us to consider alternative methods of image alignment.

### 3 IMAGE ALIGNMENT VIA CROSS-CORRELATION

The method we have developed to align multifrequency images is based on the cross-correlation technique widely used in many fields, including biomedical signal processing and imaging (Frank & McEwen 1992; Panescu 1993) and remote sensing (Hartl 1976). Cross-correlation provides a measure of how closely correlated (i.e. how alike) two functions are. The use of this measure in image alignment gives an objective, quantitative assessment of how well two images are aligned, and does not depend on the presence of very compact features. By applying different shifts between images and calculating the cross-correlation coefficient for each shift, it is possible to determine which shift results in the best alignment. The normalized cross-correlation coefficient we used (see e.g. Dunn & Clark 1974) is defined in two dimensions as

$$r_{xy} = \frac{\sum_{i=1}^n \sum_{j=1}^n (I_{v1,ij} - \bar{I}_{v1})(I_{v2,ij} - \bar{I}_{v2})}{\sqrt{\sum_{i=1}^n \sum_{j=1}^n (I_{v1,ij} - \bar{I}_{v1})^2 \sum_{i=1}^n \sum_{j=1}^n (I_{v2,ij} - \bar{I}_{v2})^2}}, \quad (1)$$

where  $n$  is the number of pixels in each direction in the two-dimensional images to be compared,  $I_{v1,ij}$  and  $I_{v2,ij}$  are the intensities for the maps at frequencies  $\nu_1$  and  $\nu_2$  at pixel (RA<sub>*i*</sub>, Dec.<sub>*j*</sub>), and  $\bar{I}_{v1}$  and  $\bar{I}_{v2}$  are the mean values of these two intensities over the region analysed. Although the source emission at a given location varies with frequency, all the radiation observed at radio frequencies is believed to be synchrotron radiation from the same population of relativistic electrons. Therefore the optically thin total-intensity ( $I$ ) structures should be well correlated despite local changes in the spectrum of the synchrotron emission due to variations in the local magnetic field, interaction with the surrounding medium and other effects. Using this (reasonable) assumption, it is possible to determine the shift to be applied between maps by comparing the structures of optically thin regions of the source at different frequencies. The highest correlation between dual-frequency images should therefore be obtained when the areas being compared correspond to the same physical region of the sky. This method has the advantage that it takes account of the optically thin emission from the *entire* source, not just isolated compact components.

### 4 IMPLEMENTATION OF THE CROSS-CORRELATION TECHNIQUE

The most widely used software for the calibration, imaging and analysis of radio interferometric data is the National Radio Astronomy Observatory AIPS (Astronomical Image Processing System) package. We have written a C program to implement the cross-correlation technique, which is external to but compatible with the NRAO AIPS package. The input to the program are two images in the format produced by the AIPS task IMTXX, and the program outputs files which can be imported back into AIPS using the task FETCH. IMTXX allows the user to export an AIPS image as a text file containing an array of floats representing the map values at each pixel location.

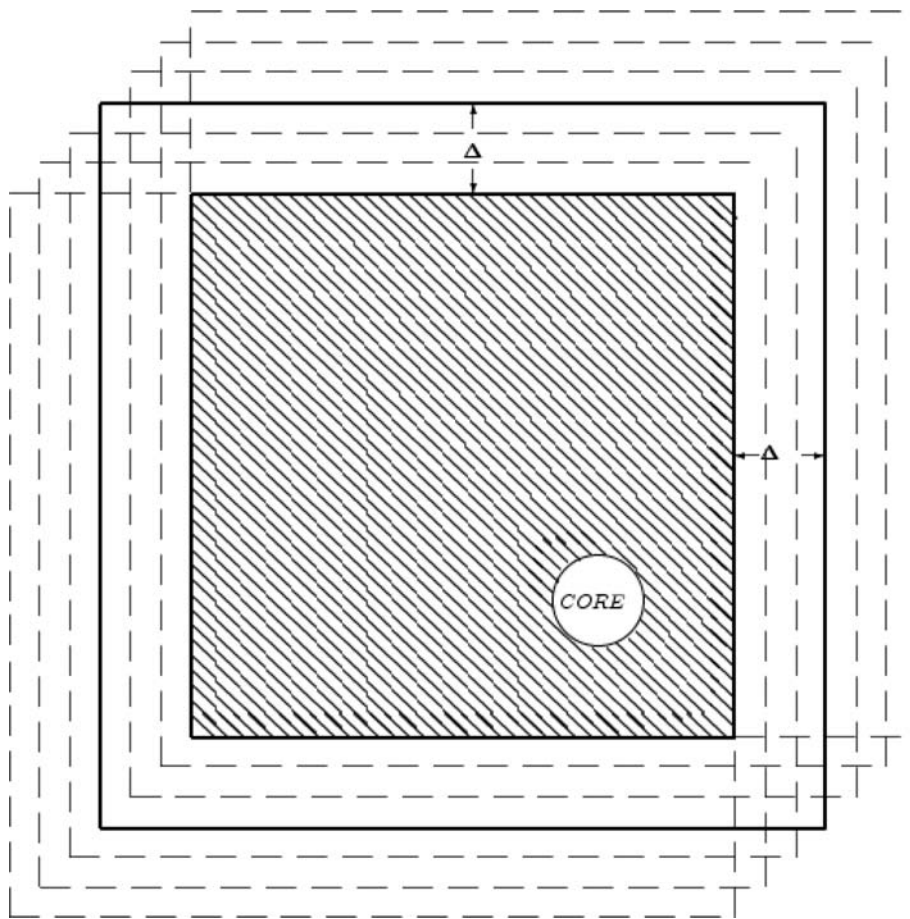


**Figure 1.** Implementation of image alignment by cross-correlation. A subarea (shaded region) of the first map (outlined in bold) is compared with the overlying region of the second map. This subarea remains constant, while the corresponding region of the second map changes as it is shifted relative to the first map (some possible shifted positions are outlined with dashed lines). The cross-correlation coefficient between the two regions, given by equation (1), is computed each time to provide a measure of how well the areas are correlated. The method assumes that the highest correlation is achieved when the areas being compared refer to the same physical region of the sky. The circle labelled ‘core’ represents a region with a specified elliptical or circular shape (corresponding to the beam shape) coincident with the position of the optically thick core, which is omitted from Map 1 during the cross-correlation calculations.

Conversely, FETCH imports a text file in the format exported by IMTXT as a map file which can be displayed by any AIPS tasks that work with images (e.g. KNTR, TVLOD).

The input images to the program must have the same pixel size and numbers of pixels (i.e. so that both the size of a pixel and the overall size of the images correspond to the same area on the sky), convolved with the same beam, and exported from AIPS using the task IMTXT. The user specifies the maximum trial shift to be applied between the images. The procedure used to calculate the shift that best aligns the input images is as follows.

(i) Strips of width  $\Delta$ , where  $\Delta$  is the maximum shift to be applied to the maps, are subtracted from each edge of the first map (Map 1). An area of the same shape as the restoring beam, but whose size is specified by the user, is removed from the area in Map 1 surrounding the (at least partially) optically thick core, whose position will be frequency dependent and which usually corresponds to the peak of the map. In comparatively unusual cases, the brightest feature may not correspond to the core; to enable the program to produce reliable results for this situation, we have included the option of the user specifying the position of the core.

(ii) The remaining area is used in the comparison (see Fig. 1). The second map (Map 2) is shifted so that different regions overlay this area each time. Since the area of Map 1 is not changed, the normalized cross-correlation coefficients can be compared directly to determine which part of Map 2 is best correlated with the selected region.

(iii) Map 2 is first shifted so that its bottom left-hand corner corresponds to the bottom left-hand corner of the selected subarea of Map 1. This corresponds to the maximum negative shift ( $-\Delta$ ,  $-\Delta$ ) applied. Map 2 is then shifted in right ascension, one pixel at a time, and the cross-correlation coefficient computed each time, until the maximum positive shift  $\Delta$  is reached. The image is then shifted by one pixel in declination, and the correlation coefficients for the next row computed in the same way. This is repeated until the maximum shift in both directions ( $\Delta$ ,  $\Delta$ ) is reached, which occurs when the top right-hand corner of Map 2 corresponds to the top right-hand corner of the selected subarea of Map 1.

(iv) The program outputs to the screen the maximum correlation  $r_{\max}$  and the shift (d RA, d Dec.) at which it occurs.

(v) Having found the best initial alignment between the two images, the program now applies the corresponding shift to

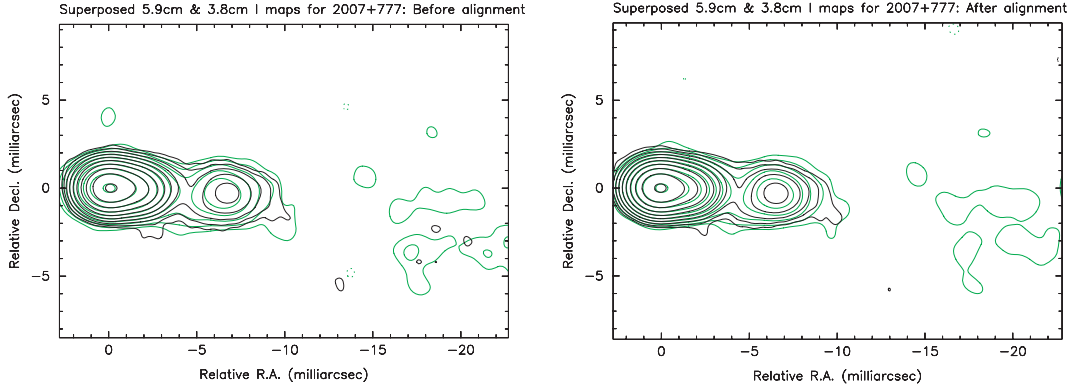


**Figure 2.** Maps of 2007+777 before (left-hand panel) and after (right-hand panel) alignment, showing the  $I$  contours at 5.1 GHz in green, with  $I$  contours at 7.9 GHz superposed in black. The convolving beam was  $1.80 \times 1.55 \text{ mas}^2$  in position angle  $87^\circ 0$ , and was the same in all cases. The bottom contour levels are  $\pm 0.20$ , and the contours increase in steps of 1.98. The peak brightness values are  $657 \text{ mJy beam}^{-1}$  (7.9 GHz) and  $547 \text{ mJy beam}^{-1}$  (5.1 GHz). The algorithm has clearly led to a very good alignment for the distinct, optically thin feature  $\simeq 7 \text{ mas}$  from the core.

Map 2, constructs a spectral-index map and blanks any optically thick points in this map, taken to be points with spectral indices  $\alpha > 0$ . The theoretical limiting optically thick spectral index  $\alpha = 5/2$  is rarely reached, but it is generally accepted that a positive spectral index implies some optically thick contribution in that region. The optically thick regions are blanked *after* first calculating the shift with only the core region blanked, since the shift between the maps can result in a significant change in the spectral-index distribution, and thus in those regions which have  $\alpha > 0$ . The cross-correlation procedure is then repeated, taking into account only the optically thin (i.e. unblanked) regions of the source, since the position of these regions is not affected by absorption effects.

(vi) The program again outputs to the screen the maximum correlation  $r_{\text{max}}$  and the shift (d RA, d Dec.) at which it occurs. Positive shifts correspond to moving the second image downward (to the south) and to the left-hand side (east) relative to the first image. In other words, a feature whose pixel location is (RA, Dec.) in the first map is located at (RA + d RA, Dec. + d Dec.) in the second map.

(vii) Three files are output. One is simply a text file containing the array of cross-correlation values computed, while the other two are text files of the format recognized by the AIPS task FETCH. One of these likewise contains the cross-correlation coefficients; importing this image into AIPS and plotting it (e.g. with KNTR) shows the shape of the cross-correlation function. The other image text file displays the subarea of Map 1 that was compared; displaying this image can be useful in verifying the area to be blanked around the optically thick core. Ideally this area should be large enough to cover virtually all of the core region, but not features in the inner jet; it should cover at least one beam size, and usually more, since the shape of the beam and the very high flux emanating from the core will dominate the VLBI  $I$  structure here.

In all cases we have tested, we found the cross-correlation function to fall off monotonically from its peak. This lends credence to the hypothesis that the optically thin jet structures in the maps should be well correlated when aligned properly (if small-scale variations were important the function could show secondary peaks where individual features align well rather than falling off uniformly, but we have never found this to be the case).

Obviously, the accuracy of the estimated shift between a pair of images will depend to some extent on the pixel size in the images being compared. In practice, it may be expedient, within reason, to

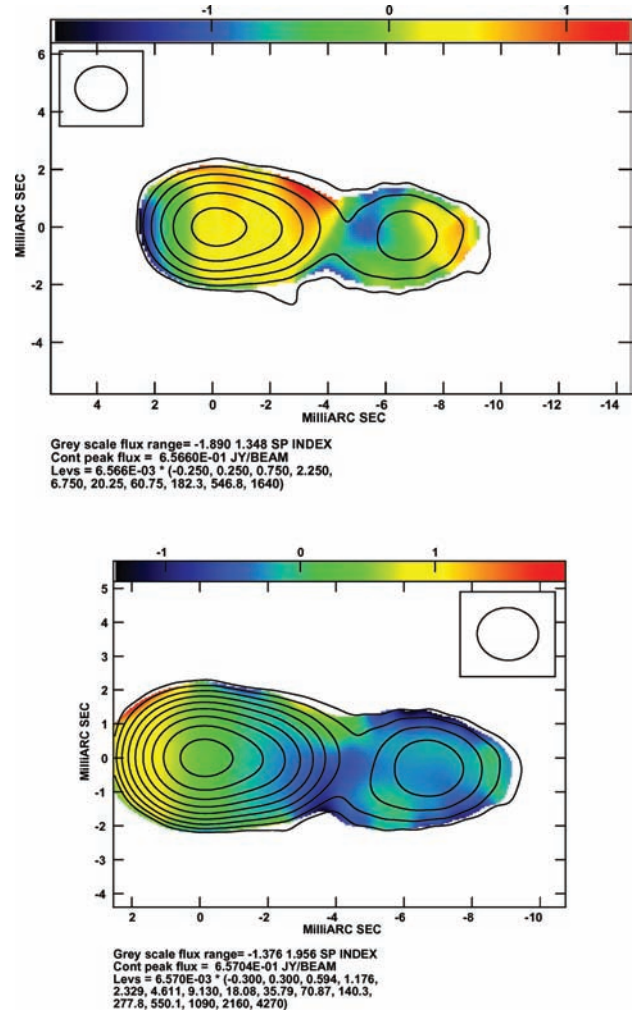


**Figure 3.** Colour spectral-index maps of 2007+777 before (top) and after (bottom) alignment, with the  $I$  contours at 7.9 GHz from Fig. 2 superposed. The convolving beam is shown in an upper corner of each image. The shown ranges of spectral indices are from  $-1.89$  to  $+1.35$  (top) and from  $-1.38$  to  $+1.96$  (bottom). Spectral artefacts due to misalignment are clearly visible in the top spectral-index map (false optically thin emission to the east of the  $I$  peak and false optically thick emission at the western end of the jet), which are absent from the bottom spectral-index map.

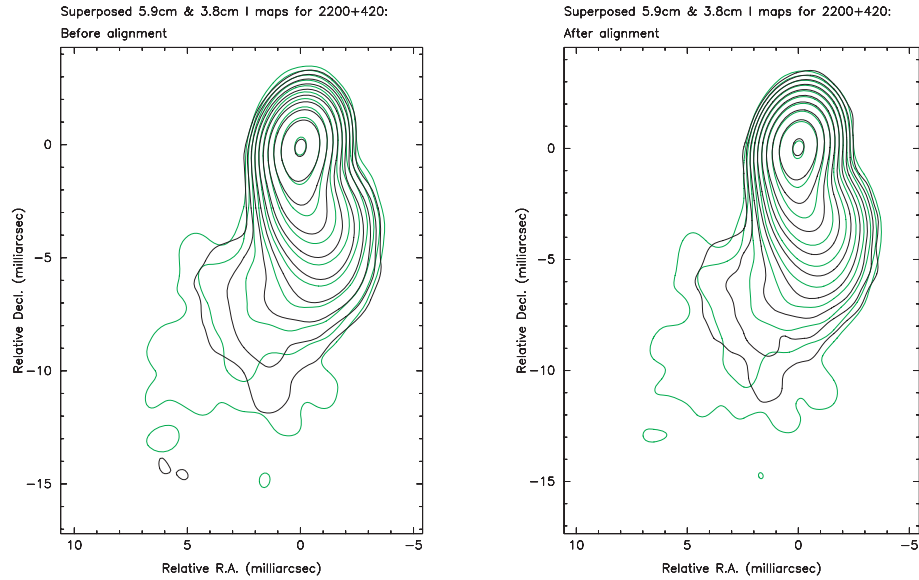


**Figure 4.** Maps of 2200+420 before (left-hand panel) and after (right-hand panel) alignment, showing  $I$  contours at 5.1 GHz in green, with  $I$  contours at 7.9 GHz superposed in black. The convolving beam was  $2.25 \times 1.59 \text{ mas}^2$  in position angle  $-13^\circ 8'$ , and was the same in all cases. The bottom contour levels are  $\pm 0.20$ , and the contours increase in steps of 1.98. The peak brightness values are  $1940 \text{ mJy beam}^{-1}$  (7.9 GHz) and  $1520 \text{ mJy beam}^{-1}$  (5.1 GHz). In this case, there is no compact, distinct optically thin feature on which to base the derived shift between the two images, but the algorithm has nevertheless properly aligned the images, as is clear from a comparison of the corresponding spectral-index maps in Fig. 5.

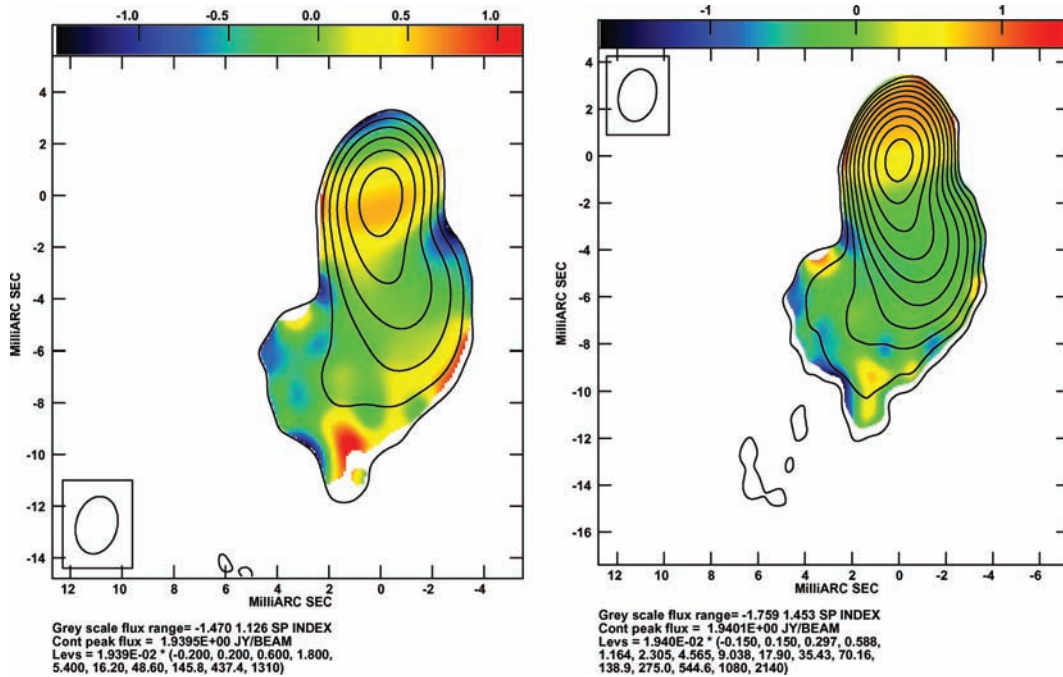


**Figure 5.** Spectral-index maps of 2200+420 before (left-hand panel) and after (right-hand panel) alignment, with the contours of total intensity at 7.9 GHz from Fig. 4 superposed. The convolving beam is shown in an upper corner of each image. The shown ranges of spectral indices are from  $-1.47$  to  $1.13$  (left-hand panel) and from  $-1.76$  to  $+1.45$  (right-hand panel). False optically thin emission is visible to the north of the  $I$  peak in the top spectral-image map. This artefact is absent from the bottom spectral-index map, and the range of spectral indices in the VLBI jet is more moderate.

use images with slightly smaller pixel sizes in order to derive more refined shift estimates. The results should not depend on whether the higher frequency or lower frequency images is used as Map 1: in either case, it is the relative shift that is being determined, and the shifts obtained with the higher frequency map as Map 1 will be the negative of those obtained with the lower frequency

map as Map 1. In practice, it may be expedient to compare results obtained blanking out core areas of several different sizes (e.g. 2.0 times the beam area, 2.5 times the beam area, etc.) to ensure that the optically thick core region is fully blanked, while as much of the optically thin inner jet is included in the correlation analysis as possible.



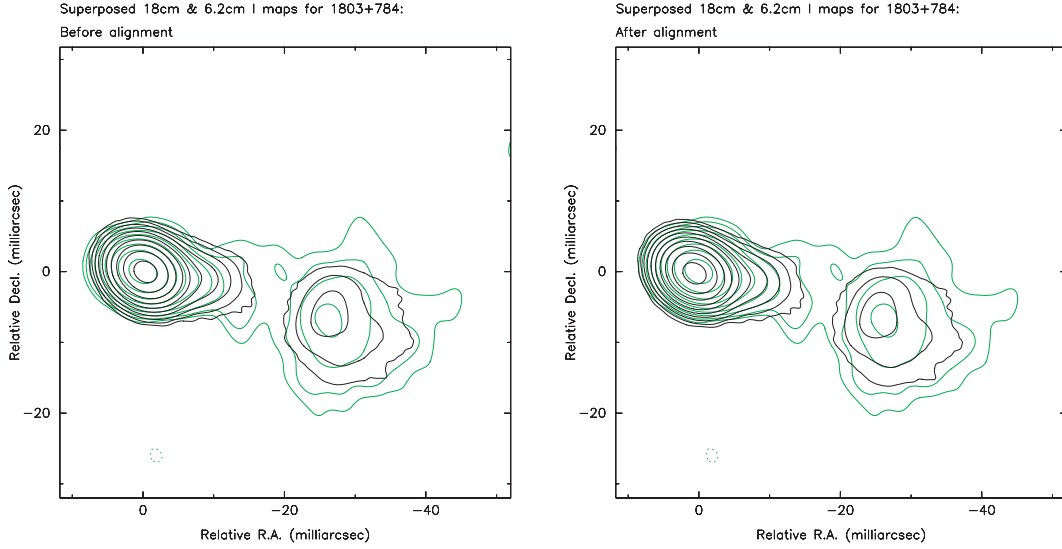


**Figure 6.** Maps of 1803+784 before (left-hand panel) and after (right-hand panel) alignment, showing  $I$  contours at 1.6 GHz in green, with  $I$  contours at 4.8 GHz superposed in black as an example of the operation of the cross-correlation technique applied to images separated by a larger frequency difference. The convolving beam for both images was  $5.49 \times 4.49 \text{ mas}^2$  in position angle  $51^\circ.2$ . The bottom contour levels are  $\pm 0.15$  (4.8 GHz) and  $\pm 0.28 \text{ mJy}$  (1.6 GHz), with the contours increasing in steps of 2.0 in both cases. The peak brightness values are  $2270 \text{ mJy beam}^{-1}$  (4.8 GHz) and  $1640 \text{ mJy beam}^{-1}$  (1.6 GHz). The 4.8- and 1.6-GHz ‘peaks’ of the somewhat diffuse jet feature roughly 25 mas from the core are at appreciably different positions in the aligned maps, but an inspection of the spectral-index maps in Fig. 7 demonstrates that the algorithm has properly aligned the overall optically thin jet structure. (Maps adapted from Gabuzda & Chernetskii 2003.)

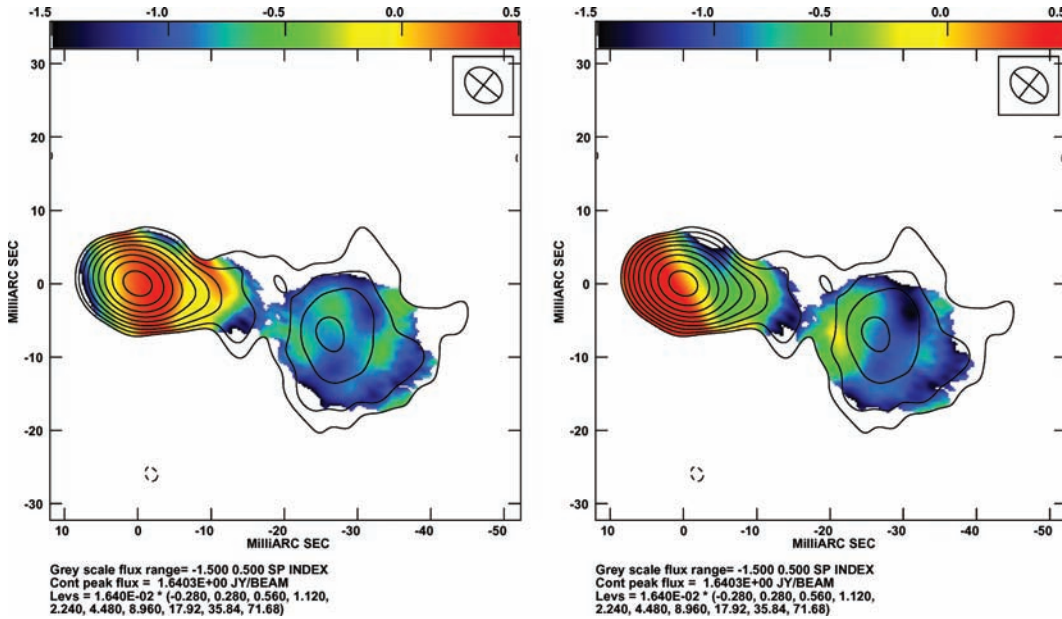


**Figure 7.** Spectral-index maps of 1803+784 before (left-hand panel) and after (right-hand panel) alignment, with the contours of total intensity at 1.6 GHz from Fig. 6 superposed. The convolving beam is shown in an upper corner of each image. The shown ranges of spectral indices are from  $-1.50$  to  $0.50$  in both cases. False optically thin emission is visible to the east of the  $I$  peak in the top spectral-image map. This artefact is absent from the bottom spectral-index map; the ‘slanting’ boundary between the regions of optically thick and thin emission near the core seems suspicious, but in fact, the initial direction of the 4.8-GHz jet on small scales is to the north-west (Gabuzda 1999).

## 5 TESTING/ILLUSTRATION OF THE CROSS-CORRELATION METHOD

We present two examples of applying the program in practice to align total-intensity images of AGN obtained with the NRAO Very Long Baseline Array at 7.9 and 5.1 GHz: (i) for 2007+777, which displays a fairly distinct optically thin jet feature that could be used to align the two maps in the ‘traditional’ way and (ii) for 2200+420,

which displays only fairly amorphous optically thin jet emission. The maps compared have matched cell sizes, map sizes and beam parameters. The VLBA observations were made over 24 h in 2006 July in a snapshot mode, so that the baseline coverage obtained was spread out over the time the sources were visible with all or nearly all of the VLBA antennas. The data were obtained simultaneously at the different frequencies. The preliminary calibration and imaging of these data were carried out in AIPS using standard techniques;

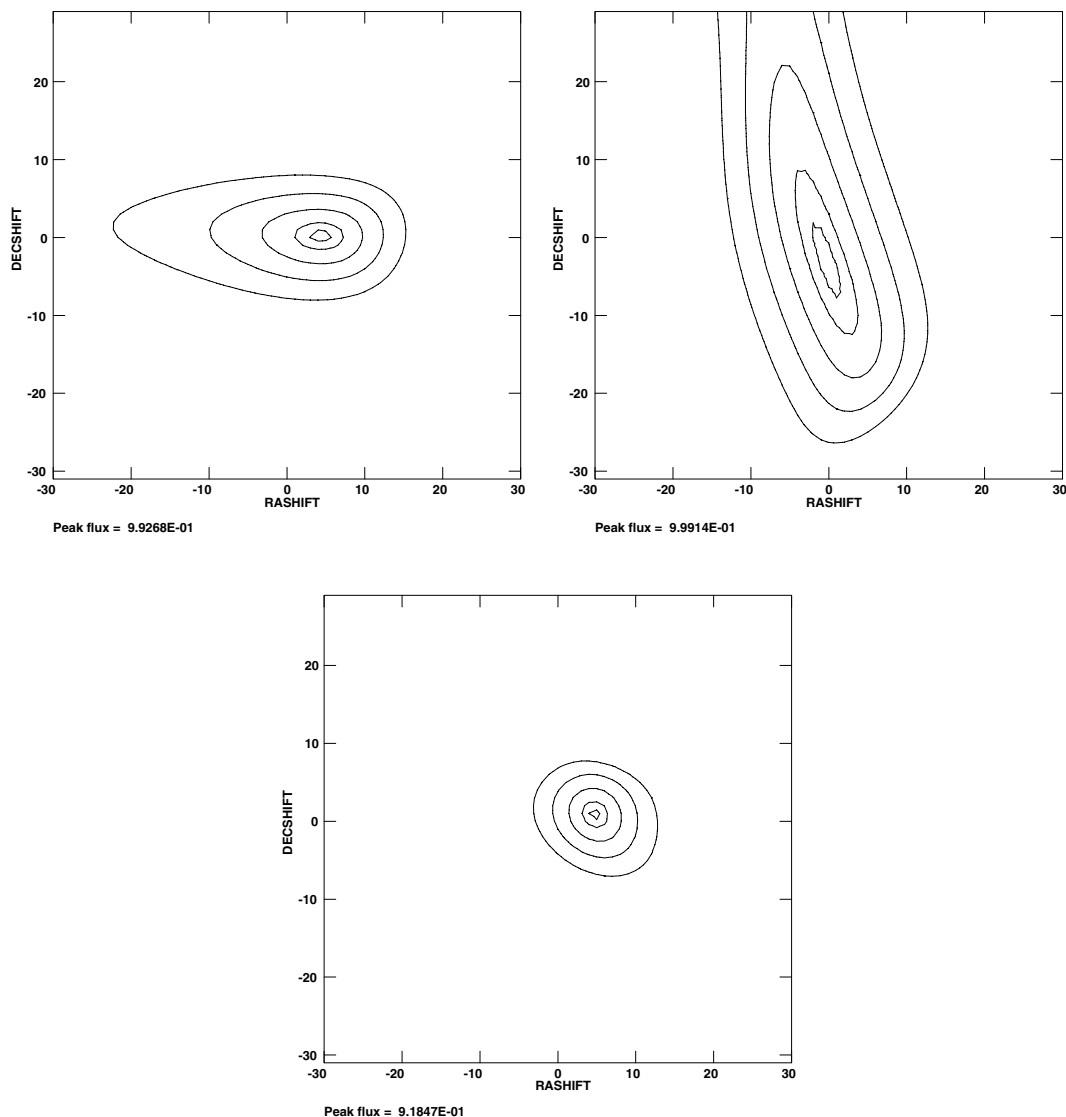


**Figure 8.** Cross-correlation functions obtained when the 7.9- and 5.1-GHz  $I$  images for 2007+777 (top left-hand panel) and 2200+420 (top right-hand panel) and 4.8- and 1.6-GHz images for 1803+784 (bottom panel) were compared. Contour levels are 90, 95, 98, 99.5, and 99.9 per cent of the peak values of 0.9927 (top right-hand panel), 0.9991 (top left-hand panel) and 0.9185 (bottom panel). The units plotted along the axes are pixels.

some initial results are presented by O’Sullivan & Gabuzda (2008), and a more complete analysis is in preparation.

For each of these two sources, we show a superposition of the 7.9- and 5.1-GHz  $I$  maps before and after applying the derived alignment shift, and the spectral-index maps obtained before and after applying the derived alignment shift (Figs 2–5). In both cases, we used a cell size of 0.1 mas during the initial total-intensity mapping, but used final maps made with a cell size of 0.05 mas as input to the program, to improve slightly the accuracy of the relative shifts obtained.

In the case of 2007+777, the derived shift of the 5.1-GHz relative to the 7.9-GHz image was 4 pixels (0.20 mas) to the west and 0 pixels to the south, in the direction of the VLBI jet, as expected. The correctness of this shift is immediately obvious via a visual inspection of the superposed  $I$  images (Fig. 2) and the spectral-index maps before and after applying this shift (Fig. 3); the algorithm has obviously aligned a distinct optically thin jet component located  $\simeq 7$  mas to the west of the map peak. In the case of 2200+420, the

calculated shift of the 5.1-GHz relative to the 7.9-GHz image was 4 pixels (0.20 mas) to the south and 0 pixels to the east, again in the direction of the VLBI jet, as expected. It is less straightforward to estimate the correctness of this shift directly from the superposed  $I$  maps in Fig. 4, but the spectral-index map after applying this shift shows appreciably more regular behaviour, with a smooth gradient in the spectral index from north of the core region to the jet extending nearly directly to the south; in particular, a spurious region of optically thin emission to the north of the peak has disappeared.

We also show the results of applying the cross-correlation technique to 4.8- and 1.6-GHz images of the AGN 1803+784 (Gabuzda & Chernetskii 2003), as an example of the operation of the program when applied to two images at more widely separated frequencies. A superposition of the 4.8- and 1.6-GHz  $I$  maps before and after applying the derived alignment shift is shown in Fig. 6, and the spectral-index maps obtained before and after applying the derived alignment shift in Fig. 7. A cell size of 0.50 mas was used during the initial total-intensity mapping, but final maps with a cell size of 0.25



mas were used as input to the shift program. The derived shift of the 1.6-GHz relative to the 4.8-GHz image was 5 pixels (1.25 mas!) to the west and 1 pixel to the north, in the direction of the VLBI jet. Although examination of the superposed *I* images (Fig. 6) does not enable an unambiguous estimate of the needed shift ‘by eye’, the correctness of the shift derived by our program is immediately obvious via a visual inspection of the spectral-index maps before and after applying this shift (Fig. 7). At first glance, the ‘slanting’ boundary between the regions of optically thick and thin emission near the core seems suspicious, but in fact, the 4.8-GHz VSOP space-VLBI image for this epoch shows that the VLBI jet initially emerges to the north-west (Gabuzda 1999), and this feature likely real (the implied spectral-index gradient is roughly perpendicular to the direction of the small-scale jet).

Finally, we show the two-dimensional plots of the cross-correlation functions output by the program for 2007+777, 2200+420 and 1803+784 (Fig. 8). The cross-correlation plots contain a single peak, with a monotonic fall-off in the correlation coefficient with distance from the derived optimal alignment shift.

## 6 CONCLUSION

We have developed a C program to determine the shift between two VLBI images based on a cross-correlation analysis of the images. In the past, it has been necessary to determine such shifts for images of AGN by aligning compact optically thin jet components, which can be a somewhat subjective and not entirely unambiguous procedure. In addition, this method is difficult to apply to complex and/or extended AGN jets without compact optically thin features suitable for such an analysis. The great advantage of our new approach is that it provides a straightforward, objective means to determine the shift between two images that makes use of all optically thin regions in the source structure, not just individual chosen features. Our tests have shown that the program produces reliable shifts for images both with and without distinct optically thin features. The code can be compiled using a standard C compiler, and has been designed to take input files written by the AIPS task IMTEXT, and to output files that can be read by the AIPS task FETCH, making it straightforward for radio astronomers familiar with AIPS to implement the code. The code can be obtained by contacting DCG (gabuzda@phys.ucc.ie).

## ACKNOWLEDGMENTS

We thank Shane P. O’Sullivan for allowing us to use unpublished images of 2007+777 and 2200+420 as examples of our alignment program, and for help in making the spectral index maps for 1803+784. SMC thanks Ger Croke for helpful discussions on the cross-correlation technique. We are also grateful to the referee, Bob Campbell, for helpful comments that led to improvement of this paper.

## REFERENCES

- Blandford R. D., Königl A., 1979, *ApJ*, 232, 34
- Boboltz D. A., 2006, in Souchay J., Feissel-Vernier M., eds, *IERS Technical Note 34*, International Celestial Reference System and Frame, Verlag des Bundesamtes für Kartographie und Geodäsie, Frankfurt am Main, p. 41
- Charlot P., 2002, in Vandenburg N. R., Baver K. D., eds, *International VLBI Service for Geodesy and Astrometry 2000, General Meeting Proceedings*. NASA/CP-2002-210002, p. 233 (<http://ivscc.gsfc.nasa.gov/publications/gm2002/charlot>)
- Cornwell T. J., Wilkinson P. N., 1981, *MNRAS*, 196, 1067
- Cotton W. D., 1979, *AJ*, 84, 1122
- Dunn O. H., Clark V. A., 1974, *Applied Statistics: Analysis of Variance and Regression*. Wiley, New York
- Fey A., 2000, in Johnston K. J., McCarthy D. D., Luzum B. J., Kaplan G. H., eds, *IAU Colloq. 180, Towards Models and Constants for Sub-Microarcsecond Astrometry*. US Naval Observatory, Washington, DC, p. 20
- Fort D. N., Yee H. K. G., 1976, *A&A*, 50, 19
- Frank J., McEwen B. F., 1992, in Frank J., ed., *Electron Tomography: Three Dimensional Imaging with the Transmission Electron Microscope*. Plenum Press, New York, p. 205
- Gabuzda D. C., 1999, *New Astron. Rev.*, 43, 691
- Gabuzda D. C., Chernetskii V. A., 2003, *MNRAS*, 229, 669
- Gabuzda D. C., Pushkarev A. B., Garnich N. N., 2001a, *MNRAS*, 327, 1
- Gabuzda D. C., Gómez J.-L., Agudo I., 2001b, *MNRAS*, 328, 719
- Hartl P., 1976, in Schanda E., ed., *Remote Sensing for Environment Sciences*. Springer-Verlag, Berlin, p. 304
- Högbom J. A., 1974, *A&AS*, 15, 417
- Lobanov A. P., 1998, *A&A*, 330, 79
- Marcaide J. M., Shapiro I. I., 1984, *ApJ*, 276, 56
- O’Sullivan S. P., Gabuzda D. C., 2008, in Rector T. A., DeYoung D. S., eds, *Extragalactic Jets: Theory and Observation from Radio to Gamma Ray*. Astron. Soc. Pac., San Francisco, in press
- Pacholczyk A. G., 1970, *Radio Astrophysics*. Freeman & Co., San Francisco
- Panescu D., 1993, in Tompkins W., ed., *Biomedical Digital Signal Processing*. Ridge Hall/Random House, New York, p. 216
- Paragi Z., Fejes I., Frey S., 2000, in Vandenburg N. R., Baver K. D., eds, *International VLBI Service for Geodesy and Astrometry 2000, General Meeting Proceedings*. NASA/CP-2000-209893, p. 342 (<http://ivscc.gsfc.nasa.gov/publications/gm2000/paragi>)
- Readhead A. C. S., Wilkinson P. N., 1978, *ApJ*, 223, 137
- Readhead A. C. S., Walker R. C., Pearson T. J., Cohen M. H., 1980, *Nat*, 285, 137
- Ros E., 2005, in Romney J., Reid M., eds, *ASP Conf. Ser. Vol. 340, Future Directions in High Resolution Astronomy: The 10th Anniversary of the VLBA*. Astron. Soc. Pac., San Francisco, p. 482

This paper has been typeset from a  $\text{\LaTeX}$  file prepared by the author.